Nanoscale heat flux between nanoporous materials

Svend-Age Biehs, Philippe Ben-Abdallah, Felipe S.S. Rosa, Karl Joulain, Jean-Jacques Greffet

▶ **To cite this version:**

Svend-Age Biehs, Philippe Ben-Abdallah, Felipe S.S. Rosa, Karl Joulain, Jean-Jacques Greffet. Nanoscale heat flux between nanoporous materials. Optics Express, 2011, 19 (S5), pp.A1088. 10.1364/OE.19.0A1088 . hal-00821584

HAL Id: hal-00821584

https://hal-iogs.archives-ouvertes.fr/hal-00821584

Submitted on 27 May 2016

HAL is a multi-disciplinary open access archive for the deposit and dissemination of scientific research documents, whether they are published or not. The documents may come from teaching and research institutions in France or abroad, or from public or private research centers.

L'archive ouverte pluridisciplinaire **HAL**, est destinée au dépôt et à la diffusion de documents scientifiques de niveau recherche, publiés ou non, émanant des établissements d'enseignement et de recherche français ou étrangers, des laboratoires publics ou privés.

Nanoscale heat flux between nanoporous materials

S.-A. Biehs,[1,*] **P. Ben-Abdallah,**[2] **F. S. S. Rosa,**[3] **K. Joulain,**[4] **and J.-J. Greffet**[5]

[1]*Laboratoire Charles Fabry, Institut d'Optique, CNRS, Université Paris-Sud, Campus Polytechnique, RD128, 91127 Palaiseau Cedex, France*
[2]*Laboratoire Charles Fabry, Institut d'Optique, CNRS, Université Paris-Sud, Campus Polytechnique, RD128, 91127 Palaiseau Cedex, France*
[3]*Laboratoire Charles Fabry, Institut d'Optique, CNRS, Université Paris-Sud, Campus Polytechnique, RD128, 91127 Palaiseau Cedex, France*
[4]*Institut P', CNRS-Université de Poitiers UPR 3346, 86022 Poitiers Cedex, France*
[5]*Laboratoire Charles Fabry, Institut d'Optique, CNRS, Université Paris-Sud, Campus Polytechnique, RD128, 91127 Palaiseau Cedex, France*

**age.biehs@institutoptique.fr*

Abstract: By combining stochastic electrodynamics and the Maxwell-Garnett description for effective media we study the radiative heat transfer between two nanoporous materials. We show that the heat flux can be significantly enhanced by air inclusions, which we explain by:(a) the presence of additional surface waves that give rise to supplementary channels for heat transfer throughout the gap, (b) an increase in the contribution given by the ordinary surface waves at resonance, (c) and the appearance of frustrated modes over a broad spectral range. We generalize the known expression for the nanoscale heat flux for anisotropic metamaterials.

References and links

1. D. Polder and M. van Hove, "Theory of radiative heat transfer between closely spaced bodies," Phys. Rev. B **4**, 3303 (1971).
2. K. Joulain, J.-P. Mulet, F. Marquier, R. Carminati, and J.-J. Greffet, "Surface electromagnetic waves thermally excited: Radiative heat transfer, coherence properties and Casimir forces revisited in the near field," Surf. Sci. Rep. **57**, 59 (2005).
3. A. I. Volokitin and B. N. J. Persson, "Near-field radiative heat transfer and noncontact friction," Rev. Mod. Phys. **79**, 1291 (2007).
4. E. A. Vinogradov and I. A. Dorofeyev, "Thermally stimulated electromagnetic fields of solids," Phys. Usp. **52**, 425 (2009).
5. M. L. Levin, V. G. Polevoi, and S. M. Rytov, "Theory of heat-transfer due to a fluctuation electromagnetic field," Sov. Phys. JETP **50**, 1054 (1980).
6. J. J. Loomis and H. J. Maris, "Theory of heat transfer by evanescent electromagnetic waves," Phys. Rev. B **50**, 18517 (1994).
7. J.-P. Mulet, K. Joulain, R. Carminati, and J.-J. Greffet, "Nanoscale radiative heat transfer between a small particle and a plane surface," Appl. Phys. Lett. **78**, 2931 (2001).
8. C. J. Fu and Z. M. Zhang, "Nanoscale radiation heat transfer for silicon at different doping levels," Int. J. Heat Mass Transfer **49**, 1703 (2006).
9. S.-A. Biehs, E. Rousseau, and J.-J. Greffet, "A mesoscopic description of radiative heat transfer at the nanoscale," Phys. Rev. Lett. **105**, 234301 (2010).
10. R. S. DiMatteo, P. Greiff, S. L. Finberg, K. A. Young-Waithe, H. K. H. Choy, M. M. Masaki, and C. G. Fonstad, "Enhanced photogeneration of carriers in a semiconductor via coupling across a nonisothermal nanoscale vacuum gap," Appl. Phys. Lett. **79**, 1894 (2001).

11. A. Kittel, W. Müller-Hirsch, J. Parisi, S.A. Biehs, D. Reddig, and M. Holthaus, "Near-field heat transfer in a scanning thermal microscope," Phys. Rev. Lett. **95**, 224301 (2005).
12. U. F. Wischnath, J. Welker, M. Munzel, and A. Kittel, "Near-field scanning thermal microscope," Rev. Sci. Instrum. **79**, 073708 (2008).
13. L. Hu, A. Narayanaswamy, X. Chen, and G. Chen, "Near-field thermal radiation between two closely spaced glass plates exceeding Planck's blackbody radiation law," Appl. Phys. Lett. **92**, 133106 (2008).
14. A. Narayanaswamy, S. Shen, and G. Chen, "Near-field radiative heat transfer between a sphere and a substrate," Phys. Rev. B **78**, 115303 (2008).
15. S. Shen, A. Narayanaswamy, and G. Chen, "Surface phonon polaritons mediated energy transfer between nanoscale gaps," Nano Lett. **9**, 2909 (2009).
16. E. Rousseau, A. Siria, G. Jourdan, S. Volz, F. Comin, J. Chevrier, and J.-J. Greffet, "Radiative heat transfer at the nanoscale," Nat. Photonics **3**, 514 (2009).
17. J. B. Pendry, "Negative refraction makes a perfect lens," Phys. Rev. Lett. **85**, 3966 (2000).
18. J. B. Pendry, "Negative refraction," Contemp. Phys. **45**, 191 (2004).
19. N. Fang, H. Lee, C. Sun, and X. Zhanget, "Sub-diffraction-limited optical imaging with a silver superlens," Science **308**, 534 (2005).
20. V. M. Shalaev, "Optical negative-index metamaterials," Nat. Photonics **1**, 41 (2007).
21. Z. Jacob, J.-Y. Kim, G. V. Naik, A. Boltasseva, E. E. Narimanov, and V. M. Shalaev, "Engineering photonic density of states using metamaterials," Appl. Phys. B **100**, 215 (2010).
22. L. Feng, Z. Liu, V. Lomakin, and Y. Fainman, "Form birefringence metal and its plasmonic anisotropy," Appl. Phys. Lett. **96**, 041112 (2010).
23. T. G. Philbin and U. Leonhardt, "Alternative calculation of the Casimir forces between birefringent plates," Phys. Rev. A **78**, 042107 (2008).
24. G. Bimonte, "Scattering approach to Casimir forces and radiative heat transfer for nanostructured surfaces out of thermal equilibrium," Phys. Rev. A **80**, 042102 (2009).
25. J. J. Saarinen, S. M. Weiss, P. M. Fauchet, and J. E. Sipe, "Reflectance analysis of a multilayer one-dimensional porous silicon structure: Theory and experiment," J. Appl. Phys. **104**, 013103 (2008).
26. J. Elser, R. Wangberg, V. A. Podolskiy, and E. E. Narimanov, "Nanowire metamaterials with extreme optical anisotropy," Appl. Phys. Lett. **89**, 261102 (2006).
27. S.-F. Chuang, S. D. Collins, and R. L. Smith, "Porous silicon microstructure as studied by transmission electron microscopy," Appl. Phys. Lett. **55**, 1540 (1989).
28. P. Halevi, A. A. Krokhin, and J. Arriaga, "Photonic crystal optics and homogenization of 2D periodic composites," Phys. Rev. Lett. **82**, 719 (1999).
29. A. A. Krokhin, P. Halevi, and J. Arriaga, "Long-wavelength limit (homogenization) for two-dimensional photonic crystals," Phys. Rev. B **65**, 115208 (2002).
30. P. Yeh, *Optical Waves in Layered Media* (Wiley, 1988).
31. The other branch is connected with the so called Brewster modes [34], that are propagating waves for which $r_{\mathrm{p,p}}$ vanishes.
32. M. Liscidini and J. E. Sipe, "Quasiguided surface plasmon excitations in anisotropic materials," Phys. Rev. B **81**, 115335 (2010).
33. A. V. Shchegrov, K. Joulain, R. Carminati, and J.-J. Greffet, "Near-field spectral effects due to electromagnetic surface excitations," Phys. Rev. Lett. **85**, 1548 (2000).
34. A. Archambault, T. V. Teperik, F. Marquier, and J.-J. Greffet, "Quantum theory of spontaneous and stimulated emission of surface plasmons," Phys. Rev. B **79**, 195414 (2009).
35. H. Raether *Surface Plasmons on Smooth and Rough Surfaces and on Gratings* (Springer-Verlag, 1988).
36. C. F. Bohren and D. R. Huffman, *Absorption and Scattering of Light by Small Particles* (John Wiley & Sons, 1983).
37. P. Ben-Abdallah and K. Joulain, "Noncontact heat transfer between two metamaterials," Phys. Rev. B **82**, 121419 (2010).
38. J. E. Sipe, "New Green-function formalism for surface optics," J. Opt. Soc. Am. B **4**, 481 (1986).
39. R. Cooke,*Classical Algebra* (John-Wiley & Sons, 2008).

1. Introduction

Near field heat transfer [1–4] between closely spaced isotropic media has been intensively studied since it has been predicted that the heat flux at nanoscale can exceed the far-field limit of the Planck's blackbody theory by orders of magnitude [5, 6]. When considering dielectrics, surface phonon polaritons provide additional enhancement as discussed in Refs. [7–9]. Several experiments have recently confirmed the theoretical predictions for simple systems [11, 13–16].

With the modern techniques of nanofabrication it is now possible to explore a whole new

level of complexity in material science and to fabricate artificial materials that can exhibit a considerable diversity of optical properties [17–22]. In many situations, these composite media possess privileged orientations so that their electromagnetic response depends on the direction of photons propagation. When the photon's wavelength in such a medium is large compared to the size of its representative unit cell, the latter behaves effectively like an anisotropic material and therefore may be described by an effective permittivity tensor (and, when necessary, an effective permeability as well). This naturally points to the question of how anisotropy influences the near-field heat transfer.

In this work, we address this question in the particular case of two semi-infinite uniaxial media characterized by optical axes orthogonally oriented with respect to the surface of interaction. The paper is organized as follows: In Sec. II we derive the expression for the heat flux between two anisotropic media. After a brief description of the relevant composite media to our purposes in Sec. III we investigate in Sec. IV the surface and Brewster modes supported by them and their main features. Next, we compare in Sec. V the near-field heat exchanges between two uniaxial media to the classical ones between two isotropic media. Finally, in order to explain the difference in the behavior of isotropic and anisotropic materials, we discuss in Sec. VI the transmission factor in detail between two uniaxial media and in Sec. VII we present our conclusions.

2. Radiative heat transfer between anisotropic media

Let B_1 and B_2 be two anisotropic semi-infinite bodies, filling respectively the regions $z<0$ and $z>d$ and leaving a vacuum gap between them. In order to ensure a stationary process, we assume that the B_i are in local thermal equilibrium at a temperature T_i, with $T_1 \neq T_2$. The heat flux P between the two bodies is given by

$$\mathrm{P}(T_1,T_2,a)=\int_{A_{12}}\mathbf{dA}\cdot\langle\mathbf{S}\rangle, \tag{1}$$

where $\mathbf{S}=\mathbf{E}\times\mathbf{H}$ is the Poynting vector and A_{12} is any surface that separates the two bodies. By taking such a surface to be a plane defined by $z=z_0\,(0<z_0<d)$ and using the (transverse) translational invariance of our system, the previous equation simplifies to

$$\mathrm{P}(T_1,T_2,a)=A\langle S_z\rangle, \tag{2}$$

showing that only the z-component of the Poynting vector is needed. After a straightforward calculation, the latter can be conveniently written as [3]

$$\langle S_z\rangle=\int_0^\infty\frac{\mathrm{d}\omega}{2\pi}\left[\Theta(\omega,T_1)-\Theta(\omega,T_2)\right]\langle S_\omega\rangle, \tag{3}$$

where we identify the mean energy of a harmonic oscillator

$$\Theta(\omega,T)=\frac{\hbar\omega}{\mathrm{e}^{\frac{\hbar\omega}{k_\mathrm{B}T}}-1}, \tag{4}$$

and also the averaged spectral Poynting vector [3]

$$\langle S_\omega\rangle=2\,\mathrm{Re}\,\mathrm{Tr}\left[\int_A\mathrm{d}\mathbf{r}'_\parallel\left(\mathbb{G}(\mathbf{r},\mathbf{r}')\partial_z\partial'_z\mathbb{G}^\dagger(\mathbf{r},\mathbf{r}')-\partial_z\mathbb{G}^\dagger(\mathbf{r},\mathbf{r}')\partial'_z\mathbb{G}(\mathbf{r},\mathbf{r}')\right)\right]_{z'=z=z_0}. \tag{5}$$

where $\mathbf{r}=\mathbf{r}_\parallel+z\hat{z}$ and $\mathbb{G}(\mathbf{r},\mathbf{r}')$ is the electrical Green's dyadic, satisfying

$$\left[\overrightarrow{\nabla}\times\overrightarrow{\nabla}\times-\frac{\omega^2}{c^2}\varepsilon(\mathbf{r},\omega)\right]\mathbb{G}(\mathbf{r},\mathbf{r}',\omega)=\delta(\mathbf{r}-\mathbf{r}')\mathbb{I}. \tag{6}$$

Moreover, we have introduced Boltzmann's constant k_B, Planck's constant $2\pi\hbar$; the † symbolizes hermitian conjugation and Tr the 3×3 trace.

In order to evaluate the heat flux in the given geometry we have to determine the Green's dyadic inside the gap region. This can be done by considering the multiple scattering of a plane wave due to a source inside the gap [23]. Details and the final expression for the Green's dyadic can be found in appendix A. When inserting the resulting expression in Eq. (40) into the heat flux formula, we find

$$\langle S_\omega \rangle = \int \frac{\mathrm{d}^2\kappa}{(2\pi)^2}\, T(\omega,\kappa;d). \tag{7}$$

The integral is carried out over all transverse wave vectors $\kappa = (k_x,k_y)^{\mathrm{t}}$ including propagating modes with $\kappa < \omega/c$ and evanescent modes with $\kappa > \omega/c$, where c is the velocity of light in vacuum. The energy transmission coefficient $T(\omega,\kappa;d)$ is different for propagating and evanescent modes and can be stated as

$$T(\omega,\kappa;d) = \begin{cases} \mathrm{Tr}\left[(\mathbb{1}-\mathbb{R}_2^\dagger\mathbb{R}_2)\mathbb{D}^{12}(\mathbb{1}-\mathbb{R}_1\mathbb{R}_1^\dagger)\mathbb{D}^{12^\dagger}\right], & \kappa < \omega/c \\ \mathrm{Tr}\left[(\mathbb{R}_2^\dagger-\mathbb{R}_2)\mathbb{D}^{12}(\mathbb{R}_1-\mathbb{R}_1^\dagger)\mathbb{D}^{12^\dagger}\right]\mathrm{e}^{-2|\gamma_{\mathrm{r}}|d}, & \kappa > \omega/c \end{cases} \tag{8}$$

where $\gamma_{\mathrm{r}} = \sqrt{\omega^2/c^2-\kappa^2}$ and $\mathbb{R}_1$, $\mathbb{R}_2$ are the 2×2 reflection matrices characterizing interfaces. By writing them a bit more explicitly,

$$\mathbb{R}_i = \begin{bmatrix} r_i^{\mathrm{s,s}}(\omega,\kappa) & r_i^{\mathrm{s,p}}(\omega,\kappa) \\ r_i^{\mathrm{p,s}}(\omega,\kappa) & r_i^{\mathrm{p,p}}(\omega,\kappa) \end{bmatrix}, \tag{9}$$

we see that their elements $r_i^{\lambda,\lambda'}$ are the reflection coefficients for the scattering of an incoming λ-polarized plane wave into an outgoing λ'-polarized wave. Note that expression (8) is very general, as it in principle applies to any crystallographic anisotropy, both electric and magnetic. In the isotropic limit they reduce to the usual Fresnel coefficients

$$\begin{aligned} r_i^{\mathrm{s,s}}(\omega,\kappa) &= \frac{\gamma_{\mathrm{r}} - \sqrt{\varepsilon_i(\omega)\omega^2/c^2-\kappa^2}}{\gamma_{\mathrm{r}} + \sqrt{\varepsilon_i(\omega)\omega^2/c^2-\kappa^2}}, \\ r_i^{\mathrm{p,p}}(\omega,\kappa) &= \frac{\varepsilon_i(\omega)\gamma_{\mathrm{r}} - \sqrt{\varepsilon_i(\omega)\omega^2/c^2-\kappa^2}}{\varepsilon_i(\omega)\gamma_{\mathrm{r}} + \sqrt{\varepsilon_i(\omega)\omega^2/c^2-\kappa^2}}, \\ r_i^{\mathrm{s,p}}(\omega,\kappa) &= r_i^{\mathrm{p,s}}(\omega,\kappa) = 0, \end{aligned} \tag{10}$$

and we see that the matrices become diagonal. In addition, we have introduced the matrix $\mathbb{D}^{12}$, defined by

$$\mathbb{D}^{12} = (\mathbb{1}-\mathbb{R}_1\mathbb{R}_2\mathrm{e}^{2\mathrm{i}\gamma_{\mathrm{r}}d})^{-1}, \tag{11}$$

which gives rise to a Fabry-Pérot-like denominator for $T(\omega,\kappa;d)$ in the isotropic case.

From Eqs. (3), (7) and (8) we see that, once the reflection matrices are known, it is possible to determine the heat flux between two arbitrary anisotropic semi-infinite bodies kept at fixed temperatures T_1 and T_2. Moreover, in order to have an independent check, we verified that Eq. (7) also can be derived from the general scattering formalism derived on Ref. [24]. In the following we will use these expressions to discuss the heat flux between two uniaxial anisotropic materials with their optical axes normal to the interface.

3. Porous materials

The structures investigated in this paper are depicted in Fig. 1. They are two semi-infinite media composed by a host isotropic material, defined by its complex dielectric function $\varepsilon_{\mathrm{h}}(\omega) =$

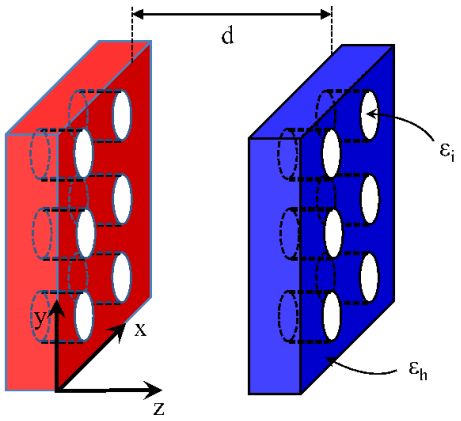

Fig. 1. Sketch of two porous slabs with different temperatures separated by a vacuum gap.

$\varepsilon_{\rm h}'(\omega)+{\rm i}\varepsilon_{\rm h}''(\omega)$ (where $\varepsilon_{\rm h}''(\omega)>0$), with uniform cylindrical inclusions oriented in the direction orthogonal to the surface as shown in Fig. 1. These inclusions in turn are filled by a medium of dielectric permittivity $\varepsilon_{\rm i}$, that is also assumed to be isotropic. When the size of the representative unit cell is much smaller than all the other characteristic scales involved, a suitable volume average of the material's local electromagnetic response can be made. In our case, the emerging azimuthal symmetry in this long wavelength limit gives rise to effective uniaxial crystals with a permittivity tensor of the form

$$\varepsilon = \varepsilon_{\parallel}\left[\mathbf{e}_x\otimes\mathbf{e}_x+\mathbf{e}_y\otimes\mathbf{e}_y\right]+\varepsilon_{\perp}\mathbf{e}_z\otimes\mathbf{e}_z \tag{12}$$

where $\mathbf{e}_x$, $\mathbf{e}_y$, and $\mathbf{e}_z$ are orthogonal unit vectors in x, y, and z direction. The parallel and perpendicular components can be derived from the Maxwell-Garnett effective medium theory (EMT) [25, 26]

$$\varepsilon_{\parallel} = \varepsilon_{\rm h}\frac{\varepsilon_{\rm i}(1+f)+\varepsilon_{\rm h}(1-f)}{\varepsilon_{\rm i}(1-f)+\varepsilon_{\rm h}(1+f)}, \tag{13}$$

$$\varepsilon_{\perp} = \varepsilon_{\rm h}(1-f)+\varepsilon_{\rm i}f, \tag{14}$$

where f is the volume fraction of inclusions. For the structure considered in this work the deviation from the exact result of homogenization given in Refs. [28, 29] is small even for relatively high filling factors such as $f=0.5$. Hence, we will discuss the heat flux between porous media with the Maxwell-Garnett expression for $f\in[0,0.5]$ in this work.

The condition of long wavelengths sets a limit to the lattice constant a of the inclusions for which the EMT can be used. In the far-field regime this condition is fullfilled when the thermal wavelength $\lambda_{\rm th}=\hbar c/k_{\rm B}T$ is much larger than a. In the near-field region the contributing modes at a distance d above the porous material have a lateral wavelength which depends on d. For $\kappa=2\pi/a$ (which corresponds to a lateral wavelength a) the evanescent waves are damped as $\exp[-\sqrt{(2\pi/a)^2-\omega^2/c^2}d]\approx\exp(-(2\pi/a)d)$ in the non-retarded near-field region above the porous material. It follows that the contribution to the heat flux is dominated by evanescent waves with lateral wavelength larger than a if $d>a/(2\pi)$. On the other hand, one can argue that a nonlocal model for the permittivity is necessary if the lateral wave vectors κ are on the order of π/a. Since the exponential in the transmission coefficient in Eq. (8) for $\kappa>\omega/c$ sets a cutoff for κ of the modes contributing to the near-field heat flux which is $\approx 1/d$, one finds that a local EMT description is permissible if $d\gg a/\pi$. Hence, for a given lattice constant a of the

inclusions the validity of the EMT in Eq. (13) in the near field regime is restricted to $d \gg a/\pi$. Artificial structures as depicted in Fig. 1 can have an a on the order of 100 nm [22] so that the distances for which the EMT can be considered as appropriate in this case are about $d > 30\,\mathrm{nm}$. Nonetheless, chemically produced nanoporous materials can show smaller structures [27] so that we will consider distances $d \in [10\,\mathrm{nm}, 100\,\mu\mathrm{m}]$.

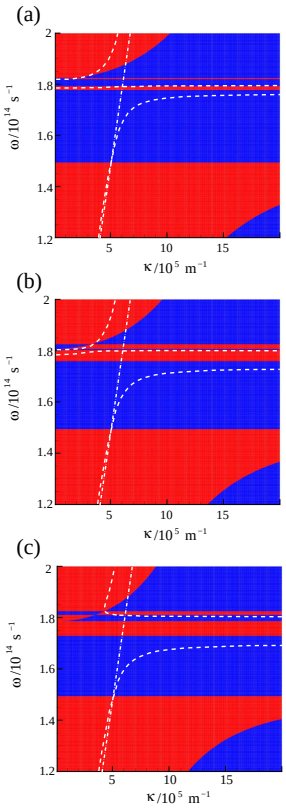

Fig. 2. Plot of the dispersion curves (white dashed lines) from Eq. (22) in the (ω,κ) plane for filling factors (a) $f = 0.1$, (b) $f = 0.3$, and (c) $f = 0.5$. The white dash-dotted line represents the light line in vacuum ($\omega = \kappa c$). Furthermore the dark (blue) areas mark the region for which γ_p is purely real, whereas the bright (red) areas are the regions for which γ_p is purely imaginary.

4. Surface and Brewster modes in porous media

Let us study the surface waves supported by these media when they are sufficiently far away from each other so that any coupling of evanescent waves can be neglected. By definition, these surface waves are resonant surface modes and therefore are determined by the poles of the reflection coefficients of these media. For out-of-plane uniaxial media the components of the

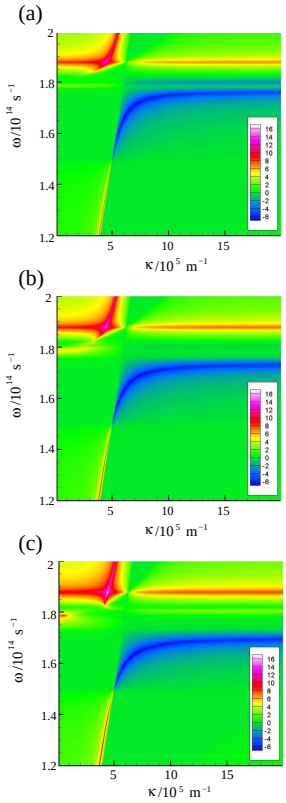

Fig. 3. Plot of $\ln(1/|r_{\mathrm{p,p}}|^2)$ in (ω,κ) plane for (a) $f=0.1$, (b) $f=0.3$, and (c) $f=0.5$.

reflection matrix are

$$r_{\mathrm{s,s}}(\omega,\kappa)=\frac{\gamma_{\mathrm{r}}-\gamma_{\mathrm{s}}}{\gamma_{\mathrm{r}}+\gamma_{\mathrm{s}}}, \tag{15}$$

$$r_{\mathrm{p,p}}(\omega,\kappa)=\frac{\varepsilon_{\parallel}\gamma_{\mathrm{r}}-\gamma_{\mathrm{p}}}{\varepsilon_{\parallel}\gamma_{\mathrm{r}}+\gamma_{\mathrm{p}}}, \tag{16}$$

$$r_{\mathrm{s,p}}=r_{\mathrm{p,s}}=0, \tag{17}$$

where $\gamma_{\mathrm{s,p}}$ are given by the solutions of Fresnel equations in the anisotropic material [30]

$$\gamma_{\mathrm{s}}=\sqrt{\varepsilon_{\parallel}\omega^2/c^2-\kappa^2}, \tag{18}$$

$$\gamma_{\mathrm{p}}=\sqrt{\varepsilon_{\parallel}\omega^2/c^2-\frac{\varepsilon_{\parallel}}{\varepsilon_{\perp}}\kappa^2}, \tag{19}$$

and hence it follows at once that the surface modes are determined by

$$(\gamma_{\mathrm{r}}+\gamma_{\mathrm{s}})=0, \tag{20}$$

$$(\varepsilon_{\parallel}\gamma_{\mathrm{r}}+\gamma_{\mathrm{p}})=0. \tag{21}$$

It is straightforward to verify that in this case only the second equation above can be satisfied, meaning that only p-polarized surface waves can exist at the interface of these media. Solving

that equation explicitly for κ gives us the sought dispersion relation of surface waves

$$\kappa = \frac{\omega}{c}\sqrt{\frac{\varepsilon_\perp(\varepsilon_\parallel - 1)}{\varepsilon_\parallel \varepsilon_\perp - 1}}. \tag{22}$$

but one must be aware that Eq. (22) has *two* branches, and only one is connected to surface modes [31]. Since their dispersion relation involves $\varepsilon_\parallel$ and $\varepsilon_\perp$, these waves are also called extraordinary surface waves [32], and they reflect the material anisotropy. When $\varepsilon_\parallel = \varepsilon_\perp = \varepsilon$, Eq. (22) degenerates into the well-known dispersion relation $\kappa = \omega/c\sqrt{\varepsilon/(\varepsilon+1)}$ of surface modes supported by a semi-infinite isotropic medium (bounded by vacuum) with a dielectric permittivity ε. In Fig. 2 we plot the dispersion curves for silicon carbide (SiC) with vacuum inclusions for different filling factors $f = 0.1$, $f = 0.3$ and $f = 0.5$. The dielectric function of SiC is described [33] by the simple model

$$\varepsilon_\mathrm{h} = \varepsilon_\infty \frac{\omega^2 - \omega_\mathrm{L}^2 - \mathrm{i}\omega\Gamma}{\omega^2 - \omega_\mathrm{T}^2 - \mathrm{i}\omega\Gamma} \tag{23}$$

where $\omega_\mathrm{L} = 1.827 \cdot 10^{14}\,\mathrm{s}^{-1}$, $\omega_\mathrm{T} = 1.495 \cdot 10^{14}\,\mathrm{s}^{-1}$, $\Gamma = 0.9 \cdot 10^{12}\,\mathrm{s}^{-1}$, and $\varepsilon_\infty = 6.7$ denote respectively the longitudinal and transversal optical phonon pulsation, the damping factor and the high frequency dielectric constant, respectively. In order to avoid the inherent difficulties of multiple possible interpretations of complex dispersion relations [34], we have deliberately neglected the host material losses to represent these curves. The relevance of this approximation can be checked by comparing Fig. 2 with Fig. 3, where we plot the reflection coefficients of dissipating porous material. In order to distinguish between evanescent and propagative waves inside the effective medium, solutions of Eq. (22) are superimposed in Fig. 2 to a two-color background. This background is a binary representation of $\zeta = \mathrm{sgn}(\varepsilon_\parallel \omega^2/c^2 - \varepsilon_\parallel \kappa^2/\varepsilon_\perp)$. In the blue zones $\zeta < 0$ so that only evanescent modes can exist, and conversely, in the red zones we have $\zeta > 0$ and all modes are propagative. Similarly the light line $\omega = c\kappa$ allows us to distinguish between the radiative (propagative) and the non-radiative (evanescent) modes inside the vacuum. Notice that, in order to satisfy Eq. (22) both ζ and $\mathrm{sgn}(\omega^2/c^2 - \kappa^2)$ must be the same. In other words, frustrated modes cannot satisfy the dispersion relation (22).

Now let us turn to the description of modes supported by our artificial structures. For low filling factors we note in Fig. 2(a) the existence of two surface modes. The first one (at a lower frequency) corresponds to the classical surface phonon-polariton (SPP) supported by a massive SiC sample [35]. That surface mode is also present in isotropic SiC. The most interesting feature of Fig. 2(a) is, however, the appearance of a second surface mode at higher frequencies, because it is a signature of the anisotropic character of the material and therefore a direct consequence of the vacuum inclusions in the host medium. As the porosity increases, both surface waves split. Beyond a critical filling factor between $f = 0.3$ and $f = 0.5$, the upper surface wave disappears as is seen in Fig. 3. Nevertheless the SPP which still exists continue to move toward the smaller frequencies, i.e., to ω_T. Above the light line, we see that the anisotropy gives rise to two different types of Brewster modes. At high frequency we recognize the usual modes where the reflection coefficient [Fig. 3(a)] of the effective medium vanishes. In addition to these modes, different Brewster modes appear depending on the value of filling factor. Also, we see on the reflection curves (Fig. 3) that the Christiansen point [36] for which the reflectivity is zero for all κ does not depend on the porosity. Indeed, an inspection of expressions (13) and (14) shows that the condition for the Christiansen point of the host material $\varepsilon_\mathrm{h} = 1$ implies that $\varepsilon_\parallel = 1$ and $\varepsilon_\perp = 1$ so that, according to Eq. (17), the reflection coefficients vanish.

5. Heat flux between porous media

Before we discuss the influence of the inclusions on the heat flux, we show in Fig. 4 the results of the mean Poynting vector $\langle S_z \rangle$ between two semi-infinite SiC bodies at fixed temperatures $T_1 = 300\,\mathrm{K}$ and $T_2 = 0\,\mathrm{K}$. First of all one can see that the heat flux becomes very large for distances much smaller than the thermal wavelength $\lambda_{\mathrm{th}} = \hbar c/k_{\mathrm{B}}T$ (which is about $7.68\,\mu\mathrm{m}$ for $T = 300\,\mathrm{K}$). At $d = 10\,\mathrm{nm}$ the heat flux for the two SiC bodies is about 1000 times larger than the heat flux between two black bodies. This increase is due to the frustrated total internal reflection and to the coupled surface phonon polariton modes [9]. In the propagating regime, i.e., for distances larger than λ_{th} the heat flux is determined by Kirchhoff-Planck's law and is limited by the black-body value. Note, that the heat flux is dominated by the p-polarized modes for distances smaller than $100\,\mathrm{nm}$ and larger than $10\,\mu\mathrm{m}$, whereas for distances in between it is dominated by the s-polarized modes.

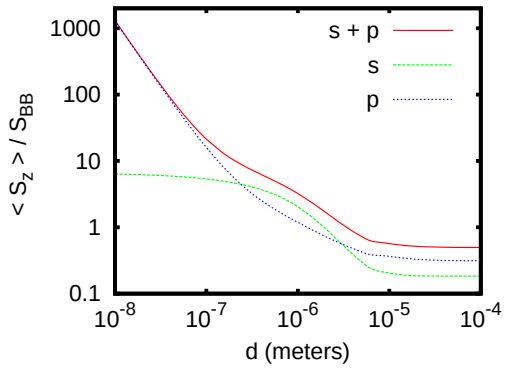

Fig. 4. Heat flux between two SiC plates over distance with $T_1 = 300\,\mathrm{K}$ and $T_2 = 0\,\mathrm{K}$. The flux is normalized to the value for two black bodies $S_{\mathrm{BB}} = 459.6\,\mathrm{Wm}^{-2}$. The contribution of the s- and p-polarized part are shown as well.

Now, we introduce the inclusions by using the Maxwell-Garnett expression in Eqs. (13) and (14). We use the same filling factor for both materials, so that we have a symmetric situation. In Fig. 5 we show the resulting heat flux normalized to the values for the two non-pourous SiC plates shown in Fig. 4. We find that for distances smaller than $100\,\mathrm{nm}$ and larger than $1\,\mu\mathrm{m}$ the heat flux becomes larger when we add air inclusions, whereas for intermediate distances the heat flux is reduced.

In order to see how the s- and p-mode contribution is changed by the porosity, we show in Fig. 6(a) and 6(b) the plots for the separate contributions of s- and p-polarized modes. It is clear that the p-polarized part of the heat flux gets enhanced for all distances when compared to the isotropic case, regardless of the filling factor. The s-polarized part in turn gives a larger heat flux for distances larger than about $1\,\mu\mathrm{m}$ and a smaller heat flux for distances smaller than $1\,\mu\mathrm{m}$. Therefore, the smaller heat flux found in Fig. 5 for intermediate distances is associated to the dominance of s-polarized modes in that distance regime.

In summary, by introducing inclusions we find for large and small distances an increase of the heat flux. For the propagating regime ($d > \lambda_{\mathrm{th}}$) this can be understood from a simple argument: the vacuum holes simply dilute the material so that, according to Kirchhoff's law, the reflectivity is decreased and hence the emissivity is increased. In fact, for $f = 1$ one would retrieve the black body result, since in this case the reflectivity is zero. On the other hand, there is no such simple argument for the increased heat flux in the near-field region. Here, it is necessary to study how the coupled surface modes, which give the main contribution to the

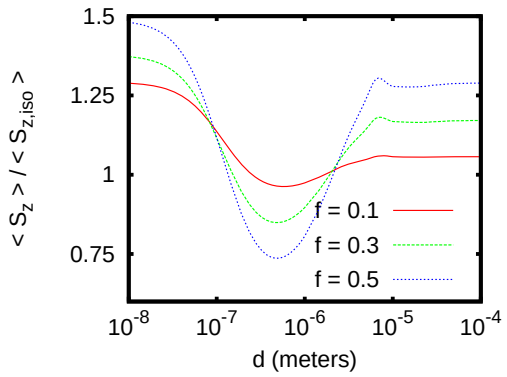

Fig. 5. Heat flux between two porous SiC plates over distance with $T_1 = 300\,\mathrm{K}$ and $T_2 = 0\,\mathrm{K}$. The flux is normalized to the value for two SiC plates shown in Fig. 4.

heat flux for distances smaller than 100 nm, are influenced by the introduction of the inclusions. This will be done by inspection of the transmission coefficient in the next section.

6. Transmission coefficient

As mentioned before, for the small distance regime ($d < 100\,\mathrm{nm}$) the heat flux between two isotropic semi-infinite SiC-bodies is solely dominated by the p-polarized contribution. This remains true for the porous SiC bodies. In fact, the dominance of the p-polarized contribution becomes even greater with increasing filling factors. Hence, to understand the observation that by introducing some porosity the heat flux becomes larger, it suffices to study the p-polarized contribution.

In Fig. 7 we show the transmission coefficient $T_\mathrm{p}(\omega,\kappa;d)$ in the (ω,κ)-plane for different filling factors and a distance $d = 100\,\mathrm{nm}$. In Fig. 7(a) one can see $T_\mathrm{p}(\omega,\kappa;d)$ for two isotropic SiC plates. Here, $T_\mathrm{p}(\omega,\kappa;d)$ is one or close to one for the propagating modes, the total internal reflection modes and the coupled surface phonon polaritons. In the plotted region one can mainly see the coupled surface phonon polaritons, which are responsible for the large heat flux at small distances. Now, for $f = 0.1$ one can see in Fig. 7(b) that a second coupled surface mode appears due to the air inclusions. In addition, the coupled surface mode of the bulk SiC is shifted to smaller frequencies. When increasing the filling factor [Fig. 7(c) and 7(d)] the upper coupled surface modes shift to higher frequencies and become less important for the transmission coefficient. On the other hand, the low frequency surface modes shift further to lower frequencies. Between the two coupled surface mode branches a band of frustrated internal reflection modes is formed which gives also a non-negligible contribution to the transmission coefficient.

In order to get further information we now consider the spectral mean Poynting vector $\langle S_\omega \rangle$ defined in Eq. (7) for p-polarization only. We have plotted this quantity in Fig. 8 at the same distance as before, i.e., $d = 100\,\mathrm{nm}$, and again for different filling factors. As in Fig. 7 one can see the strong contribution of the two coupled surface mode resonances, which are shifted in frequencies when changing the filling factor. Moreover, the shifting of the primary surface mode to lower frequencies by itself also enhances the flux, as such a shift brings that surface mode closer to the peak wavelength of blackbody radiation as given by the Wien's law. Furthermore, one can now observe, that when increasing the filling factor the low frequency resonance is not only shifted to smaller frequencies, but the resonance is also getting stronger.

The study can now be completed when considering the mean transmission factor for the

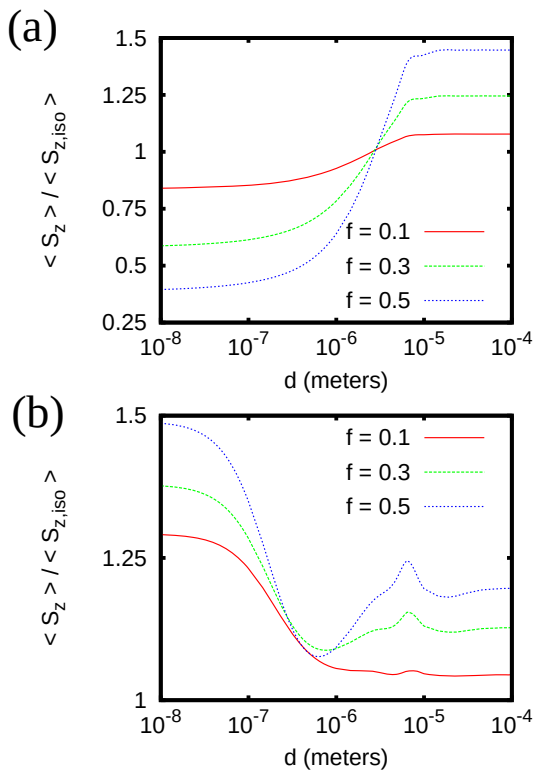

Fig. 6. As in Fig 5 but for the (a) s- and (b) p-polarized contribution only.

p-polarized modes, that was introduced in Ref. [9] as

$$\overline{T}_{\mathrm{p}}(\kappa) = \frac{3}{\pi^2}\int_0^\infty \mathrm{d}u\, f(u) T_{\mathrm{p}}(u,\kappa;d) \tag{24}$$

with $u = \hbar\omega/k_{\mathrm{B}}T$ and $f = u^2 \mathrm{e}^u/(e^u-1)^2$. It represents the mean transmission coefficient of a mode specified by it's wave vector κ for a given temperature T and a small temperature difference ΔT between the two bodies. By means of this quantity the heat flux can be rewritten in a Landauer-like form [9]

$$\langle S_z\rangle = \frac{\pi^2}{3}\frac{k_{\mathrm{B}}^2 T}{h}\int\frac{\mathrm{d}\kappa}{2\pi}\,\kappa\,\overline{T}_{\mathrm{p}}(\kappa)\Delta T. \tag{25}$$

Note, that for $\kappa d \gg 1$ and $\kappa > \omega/c$ the transmission coefficient $T_{\mathrm{p}}(\omega,\kappa;d)$ is exponentially damped [see Eq. (8)] and therefore also the mean transmission factor $\overline{T}_{\mathrm{p}}(\kappa)$. This damping determines the wave vector cutoff and hence the number of states contributing to the heat flux.

Now, in Fig. 9 we plot $\overline{T}_{\mathrm{p}}(\kappa)$ for a given distance of $d = 100\,\mathrm{nm}$ and different filling factors normalized to the mean transmission factor for two semi-infinite SiC bodies. For $f = 0.1$ the mean transmission coefficient for the porous SiC increases for intermediate κ but decreases for very large κ. The increased mean transmission factor is due to the second coupled surface mode and the frustrated modes, whereas the lower value for large wave vectors can be attributed to a stronger cutoff in the transmission coefficient, which means that the number of contributing modes is decreased. The enhancement of the transmission factor due to the surface mode prevails and leads to an enhanced heat flux at that distance. The same mechanism is responsible for

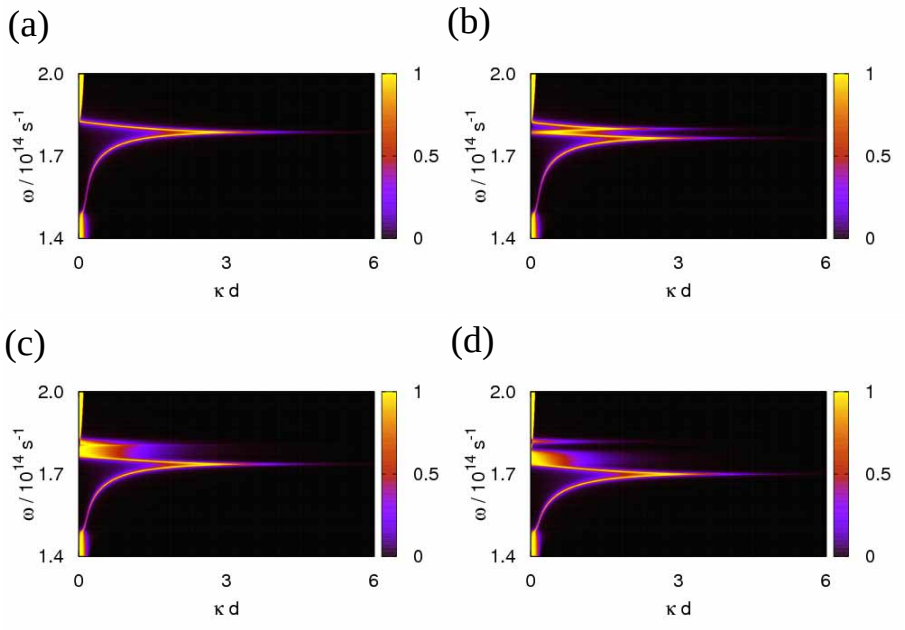

Fig. 7. Transmission coefficient $T_{\mathrm{p}}(\omega,\kappa;d)$ in the (ω,κ)-plane for two porous SiC slabs with different filling factors (a) $f=0$, (b) $f=0.1$, (c) $f=0.3$, and (d) $f=0.5$. The distance is fixed at $d=100\,\mathrm{nm}$.

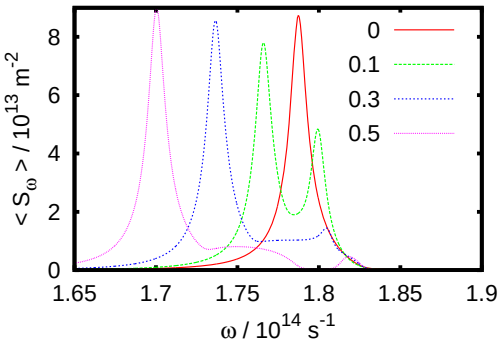

Fig. 8. Spectral mean Poynting vector $\langle S_\omega \rangle$ defined in Eq. (7) for two porous SiC slabs with different filling factors $f=0,0.1,0.3,0.5$ considering only the p-polarized contribution. The distance is fixed at $d=100\,\mathrm{nm}$.

the enhanced heat flux for $f=0.3$. On the other hand, for larger filling factors the curves change slightly for intermediate κ compared to the curve for $f=0.3$. The contribution in that intermediate region is due to the second coupled surface mode branch and the frustrated modes. But for very large κ the mean transmission coefficient increases compared to $f=0.3$. This means that by introducing a higher porosity we soften the cutoff of the transmission coefficient. Hence, the number of modes contributing to the heat flux is increased and results for large filling factors in a further enhanced heat flux.

The dependence of the cutoff on the filling factor for large κ can easily be discussed for the

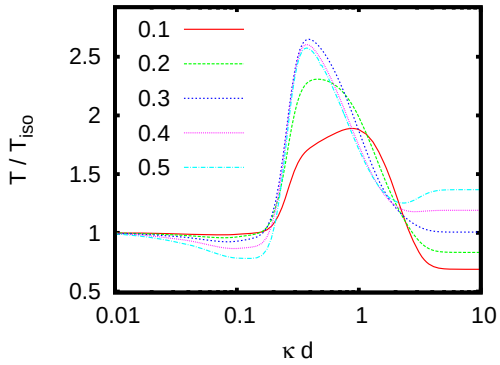

Fig. 9. Mean transmission coefficient defined in Eq. (24) for different filling factors normalized to the isotropic case ($f = 0$). The distance is fixed at $d = 100\,\mathrm{nm}$ and the temperature at $T = 300\,\mathrm{K}$.

transmission coefficient $T_\mathrm{p}(\kappa,\omega;d)$. It was found in Ref. [9] that the cutoff region, i.e., where $T_\mathrm{p}(\kappa,\omega;d)$ is exponentially damped, is given by

$$\kappa_\mathrm{iso} > \log\left(\frac{2}{\mathrm{Im}(\varepsilon)}\right)\frac{1}{2d} \tag{26}$$

when considering two isotropic semi-infinite bodies at the surface mode resonance frequency [see also Refs. [37]]. For the uniaxial anisotropic case as considered here, this relation changes to

$$\kappa_\mathrm{uni} > \log\left(\frac{2}{\mathrm{Im}(\sqrt{\varepsilon_\parallel\varepsilon_\perp})}\right)\frac{1}{2d} \tag{27}$$

where the permittivities have to be evaluated at the surface mode resonance frequency of the semi-infinite anisotropic body (see Appendix B). In Fig. 10 we show a plot of $\kappa_\mathrm{uni}/\kappa_\mathrm{iso}$ over the filling factor. It is seen that by introducing the air inclusions the cutoff first decreases and then monotonically increases. This is the same qualitative behavior as observed for the mean transmission factor $\overline{T}_\mathrm{p}(\kappa)$ in Fig. 9 for $\kappa d \gg 1$. This reasoning confirms that the number of contributing modes is the main mechanism for increasing the heat flux at small distances and large filling factors ($f > 0.3$).

7. Conclusion

We have presented a detailed study of near and far field heat transfer between two flat uniaxial media made of polar materials (in our case, SiC) in which cylindrical inclusions drilled orthogonally to surfaces are uniformally distributed.

After applying the classical stochastic electrodynamic theory to anisotropic materials we have shown that, for short distances, the heat flux between such media can be significantly larger than those traditionally measured between two isotropic materials in the same non-equilibrium thermal conditions. For small filling factors we have determined that this enhancement stems from additional surface waves arising at the uniaxial material-vacuum interface, clearly indicating that such increase is intrinsically connected to anisotropy. Indeed, we did calculations for isotropically rarified SiC plates with low filling factors ($f \leq 0.1$) and found that the heat transfer modification for is much smaller. In contrast, for larger filling factors ($f > 0.3$) we have shown that, after a thorough analysis of the transmission factor, the enhancement in heat transfer arises mainly from the increased number of modes contributing to the flux.

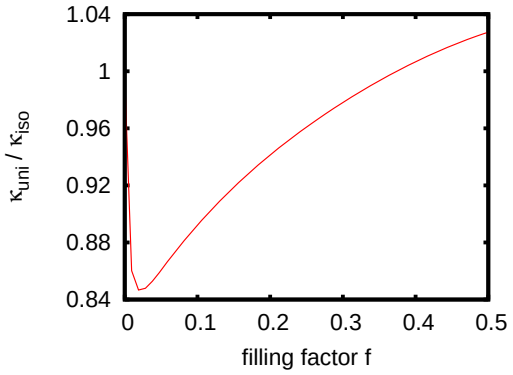

Fig. 10. Plot of the normalized cutoff value $\kappa_{\mathrm{uni}}/\kappa_{\mathrm{iso}}$ over filling factor f.

A. Green's dyadic in the gap region

In order to construct the Green's dyadic in the vacuum gap we first start with the Green's dyadic in free space. If $z > z'$ Weyl's expansion for the Green's dyadic is [38]

$$\mathbb{G}(\mathbf{r},\mathbf{r}') = \int \frac{\mathrm{d}^2\kappa}{(2\pi)^2} \frac{\mathrm{i}e^{\mathrm{i}\kappa\cdot(\mathbf{x}-\mathbf{x}')}}{2\gamma_{\mathrm{r}}} e^{\mathrm{i}\gamma_{\mathrm{r}}(z-z')}\mathbb{1} \tag{28}$$

with $\gamma_{\mathrm{r}} = \sqrt{\omega^2/c^2 - \kappa^2}$, $\mathbf{x} = (x,y)^{\mathrm{t}}$ and $\kappa = (k_x,k_y)^{\mathrm{t}}$. The unit dyadic $\mathbb{1}$ is the unit dyadic in the polarization basis and is defined as

$$\mathbb{1} = \hat{\mathbf{a}}_{\mathrm{s}}^{+} \otimes \hat{\mathbf{a}}_{\mathrm{s}}^{+} + \hat{\mathbf{a}}_{\mathrm{p}}^{+} \otimes \hat{\mathbf{a}}_{\mathrm{p}}^{+}. \tag{29}$$

The polarisation vectors for s- and p-polarized waves are given by

$$\hat{\mathbf{a}}_{\mathrm{s}}^{+} = \frac{1}{\kappa}\begin{pmatrix} -k_y \\ k_x \\ 0 \end{pmatrix} \qquad \text{and} \qquad \hat{\mathbf{a}}_{\mathrm{p}}^{+} = \frac{c}{\kappa\omega}\begin{pmatrix} k_x\gamma_{\mathrm{r}} \\ k_y\gamma_{\mathrm{r}} \\ -\kappa^2 \end{pmatrix}. \tag{30}$$

By construction both polarization vectors are orthogonal. For propagating waves they are also normalized. The Fourier component $\mathbb{G}(\kappa;z,z')$ of the Greens dyadic is defined by

$$\mathbb{G}(\mathbf{r},\mathbf{r}') = \int \frac{\mathrm{d}^2\kappa}{(2\pi)^2}\, \mathbb{G}(\kappa;z,z')\, e^{\mathrm{i}\kappa\cdot(\mathbf{x}-\mathbf{x}')}. \tag{31}$$

The above expression for the Green's dyadic represents the field of a right going wave at z of a source of unit strength placed at z'. If a semi-infinite medium is located at $z > d$ then this wave will be reflected so that the Green's dyadic $\mathbb{G}(\kappa;z,z')$ reads at $z > z'$

$$\mathbb{G}_A(\kappa;z,z') = \frac{\mathrm{i}}{2\gamma_{\mathrm{r}}}\left[\mathbb{1}e^{\mathrm{i}\gamma_{\mathrm{r}}(z-z')} + e^{2\mathrm{i}\gamma_{\mathrm{r}}d}e^{\mathrm{i}\gamma_{\mathrm{r}}(z+z')}\mathbb{R}_2\right] \tag{32}$$

where we have introduced the reflection matrix

$$\mathbb{R}_2 = \sum_{i,j=\{\mathrm{s,p}\}} r_{i,j}^2\, \hat{\mathbf{a}}_i^{-} \otimes \hat{\mathbf{a}}_j^{+} \tag{33}$$

with the reflection coefficients $r^2_{i,j}$ and the polarization vectors $\hat{\mathbf{a}}^-_p = -c/(\kappa\omega)(k_x\gamma_r, k_y\gamma_r, \kappa^2)^t$ and $\hat{\mathbf{a}}^-_s = \hat{\mathbf{a}}^+_s$. If there is now a second semi-infinite medium at $z < 0$ with a reflection operator defined as

$$\mathbb{R}_1 = \sum_{i,j=\{s,p\}} r^1_{i,j} \hat{\mathbf{a}}^+_i \otimes \hat{\mathbf{a}}^-_j \tag{34}$$

the waves in that cavity will be multiply reflected at the boundaries at $z = 0$ and $z = d$ so that [23]

$$\begin{aligned}\mathbb{G}_A(\kappa; z, z') = \frac{i}{2\gamma_r}\Big[&\mathbb{1}e^{i\gamma_r(z-z')} + e^{2i\gamma_r d}e^{-i\gamma_r(z+z')}\mathbb{R}_2 \\ &+ e^{2i\gamma_r d}e^{i\gamma_r(z-z')}\mathbb{R}_1\mathbb{R}_2 \\ &+ e^{4i\gamma_r d}e^{-i\gamma_r(z+z')}\mathbb{R}_2\mathbb{R}_1\mathbb{R}_2 + \ldots\Big].\end{aligned} \tag{35}$$

Summing up all contributions we get

$$\mathbb{G}_A(\kappa; z, z') = \frac{i}{2\gamma_r}\left[\mathbb{D}^{12}e^{i\gamma_r(z-z')} + \mathbb{D}^{21}\mathbb{R}_2 e^{2i\gamma_r d}e^{-i\gamma_r(z+z')}\right] \tag{36}$$

where we have introduced

$$\mathbb{D}^{12} = (\mathbb{1} - \mathbb{R}_1\mathbb{R}_2 e^{2i\gamma_r d})^{-1}, \tag{37}$$

$$\mathbb{D}^{21} = (\mathbb{1} - \mathbb{R}_2\mathbb{R}_1 e^{2i\gamma_r d})^{-1}. \tag{38}$$

The expression in Eq. (36) is not yet the complete intracavity Green's dyadic, since we have not considered the waves which start from z' as left going waves and arrive after being reflected at the boundary at $z = 0$ at $z > z'$. With the same reasoning as for $\mathbb{G}_A(\kappa; z, z')$ we find for this contribution

$$\mathbb{G}_B(\kappa; z, z') = \frac{i}{2\gamma_r}\left[\mathbb{D}^{12}\mathbb{R}_1 e^{i\gamma_r(z+z')} + \mathbb{D}^{21}\mathbb{R}_2\mathbb{R}_1 e^{2i\gamma_r d}e^{i\gamma_r(z'-z)}\right] \tag{39}$$

Finally, the intracavity Green's dyadic is given by the sum of Eqs. (36) and (39) yielding

$$\begin{aligned}\mathbb{G}_{\text{intra}} = \frac{i}{2\gamma_r}\Big[&\mathbb{D}^{12}\left(\mathbb{1}e^{i\gamma_r(z-z')} + \mathbb{R}_1 e^{i\gamma_r(z+z')}\right) \\ &+ \mathbb{D}^{21}\left(\mathbb{R}_2\mathbb{R}_1 e^{i\gamma_r(z'-z)}e^{2i\gamma_r d} + \mathbb{R}_2 e^{2i\gamma_r d}e^{-i\gamma_r(z+z')}\right)\Big]\end{aligned} \tag{40}$$

B. The resonances in an anisotropic material

The precise location of resonances can be analytically determined from expression (22) by solving

$$\varepsilon_\parallel \varepsilon_\perp = 1. \tag{41}$$

Frequencies which satisfy this condition are resonance frequencies of medium because they correspond to a flat region of the dispersion curve in the (ω, κ) plane and therefore to strong density of states. Using expressions (13) and (14) this equation can be recast into the following form

$$a\varepsilon_h^3 + b\varepsilon_h^2 + c\varepsilon_h + d = 0, \tag{42}$$

with

$$a = (1-f)^2, \tag{43}$$
$$b = \varepsilon_{\mathrm{i}}(1-f)(2f+1), \tag{44}$$
$$c = (1+f)(\varepsilon_{\mathrm{i}}^2 f - 1), \tag{45}$$
$$d = \varepsilon_{\mathrm{i}}(f-1). \tag{46}$$

The solutions of this equation can readily been calculated using the Cardano's method [39]. When inclusions are made by pure vacuum (i.e. $\varepsilon_{\mathrm{i}} = 1$), these solutions are real and read

$$\varepsilon_{h,n} = 2\sqrt{\frac{-p}{3}}\cos\left[\frac{1}{3}\arccos\left(-\frac{q}{2}\sqrt{\frac{27}{-p^3}}\right) + \frac{2\pi n}{3}\right] \tag{47}$$

for $n = 0, 1, 2.$ with

$$p = \frac{3ac - b^2}{3a^2} \qquad \text{and} \qquad q = \frac{27a^2d - 9abc + 2b^3}{27a^3} \tag{48}$$

Only one of these solutions is positive and must be conserved to search the resonance frequencies.

Acknowledgments

We thank Henri Benisty for very helpful discussions on the subject of homogenization. S.-A. B. gratefully acknowledges support from the Deutsche Akademie der Naturforscher Leopoldina (Grant No. LPDS 2009-7). This research was partially supported by Triangle de la Physique, under the contract 2010-037T-EIEM.